

See discussions, stats, and author profiles for this publication at: <https://www.researchgate.net/publication/272563466>

Magnetostructural dynamics of Rieske versus ferredoxin iron–sulfur cofactors

ARTICLE *in* PHYSICAL CHEMISTRY CHEMICAL PHYSICS · FEBRUARY 2015

Impact Factor: 4.49 · DOI: 10.1039/c4cp05465b

READS

33

3 AUTHORS, INCLUDING:



[Md. Ehesan Ali](#)

Institute of Nano Science and Technology

26 PUBLICATIONS 515 CITATIONS

SEE PROFILE



Cite this: *Phys. Chem. Chem. Phys.*,
2015, 17, 6289

Magnetostructural dynamics of Rieske *versus* ferredoxin iron–sulfur cofactors

Md. Ehesan Ali,* Volker Staemmler and Dominik Marx

The local chemical environment of the [2Fe–2S] cofactor hosted by ferredoxin and Rieske-type proteins is fundamentally different due to the presence of distinct ligands at the two iron centers in the case of Rieske proteins, whereas they are identical in ferredoxins. This renders Rieske [2Fe–2S] cores chemically asymmetric and results in more complex vibrational spectra as compared to ferredoxin. Likewise, one would expect other properties, for instance the dynamics of the magnetic exchange coupling constant J , to be also more complex. Applying *ab initio* molecular dynamics using our recently introduced spin-constrained two-determinant extended broken symmetry (CEBS) approach to Rieske and ferredoxin model complexes at 300 K, we extract the molecular fluctuations and the resulting magnetostructural cross-correlations involving the antiferromagnetic exchange interaction $J(t)$. This analysis demonstrates that the details of the magnetostructural dynamics are indeed distinctly different for Rieske and ferredoxin cofactors, while the time averages of $\langle J \rangle$ are shown to be essentially identical. In particular, the frequency window between about 200 and 350 cm^{-1} , is a “fingerprint region” that allows one to distinguish chemically asymmetric from symmetric cofactors and thus Rieske proteins from ferredoxins.

Received 24th November 2014,
Accepted 26th January 2015

DOI: 10.1039/c4cp05465b

www.rsc.org/pccp

1 Introduction

Iron–sulfur proteins play a vital role in various physiological processes such as respiration, energy conversion, and electron transport to name but a few.^{1–5} Important members of the family of iron–sulfur proteins are ferredoxin and Rieske-type proteins, the fundamental difference between them being the local coordination environment of the two iron centers in the [2Fe–2S] cofactors.^{4,6–8} In ferredoxins each Fe center is coordinated with two cysteines *via* Fe–S bonds, whereas in Rieske proteins only one of the two Fe atoms in the [2Fe–2S] core is coordinated with two cysteines, whereas the other Fe site is covalently bound with Fe–N bonds to two histidine residues. As a result of this local embedding within the protein matrix, a chemical asymmetry is established in Rieske-type iron–sulfur cores which is absent in ferredoxins (see ref. 9 and literature cited therein).

In the oxidized states of these two different proteins, the oxidation state of each Fe center becomes +3 thus leading to a d^5 system with five unpaired electrons at each iron site. The two spin-bearing iron centers are coupled to each other through a superexchange-driven antiferromagnetic coupling mechanism where the bridging sulfides (S^{2-}) play a crucial role in mediating the exchange mechanism.^{10–15} The strengths of these magnetic exchange couplings are governed by various magnetostructural

factors in addition to the celebrated Goodenough–Kanamori rules,^{16,17} such as factors that influence the local spin moments.^{18–21} As a consequence, at finite temperature, the fluctuations of the magnetic properties intrinsically and sensitively account for the dynamics of the coupled spin centers. Obviously, the dynamical cross-correlations between magnetic properties and molecular structure will remain inaccessible to any static calculation irrespective of the choice of electronic structure theory – unless explicit dynamics is performed based on forces that are obtained consistently from electronic structure calculations. Such fully dynamical techniques have been developed in recent years in the framework of *ab initio* molecular dynamics (AIMD)²² and have been applied successfully to various [2Fe–2S] systems.^{9,21,23–26}

In the present study, we ask the question to what extent the magnetostructural dynamics of the [2Fe–2S] cofactor differs in chemically asymmetric Rieske proteins in comparison to chemically symmetric ferredoxins using finite model complexes at ambient temperature.

2 Methods

In order to generate the magnetostructural dynamics of such iron–sulfur clusters, which requires computationally demanding AIMD simulations²² to be carried out, we have adopted a density-based rather than a wave function-based approach. However, the major challenge in any density-based approach

Lehrstuhl für Theoretische Chemie, Ruhr-Universität Bochum, 44780 Bochum, Germany. E-mail: ehesan.ali@theochem.rub.de

to magnetic interactions is to describe the antiferromagnetic spin ground state of the [2Fe-2S] clusters, as it possesses a significant amount of multi-reference character. Clearly, wavefunction-based multi-reference methods are, in principle, highly desirable on one hand, but become quickly unfeasible if many electrons need to be fully correlated on the other hand. A computationally much less demanding alternative route to the problem is the spin-projected broken-symmetry (BS) density functional theory approach proposed by Noodleman.^{27–29} Clearly, the single-determinant broken-symmetry wavefunction itself is not a reasonable approximation for the low-spin (LS) antiferromagnetic state, rather it is a spin-symmetry broken state that can be utilized to extract the magnetic exchange interaction J upon suitable spin-projection based on the eigenstates of Heisenberg's spin Hamiltonian (which must be approximately valid for the particular system of interest). A while ago we extended the original approach to a fully coupled two-determinant framework, the so-called extended broken-symmetry method (EBS), that enables a formally consistent description of the properties of antiferromagnetic ground states in terms of an approximate LS potential energy surface and thus allows for AIMD by generating that LS surface “on the fly”.^{23,24} The magnetic exchange coupling constants J are accessed at each timestep by propagating the coupled high-spin (HS) and broken-symmetry (BS) Kohn–Sham determinants simultaneously in the construction of multi-determinant Born–Oppenheimer or Car–Parrinello approaches. For details related to the EBS method we refer the readers of our previous works^{9,21,23–26} as well as to follow-up studies of others groups.²⁰ Thus, we summarize in the following only the salient features of the methodology that is applied in the current work by following ref. 21, where comprehensive background can be found.

2.1 Calculation of the magnetic exchange coupling

The magnetic exchange interaction of the two iron atoms in a [2Fe-2S] cluster can be expressed using Heisenberg's spin Hamiltonian,

$$\hat{H} = -2J\hat{S}_{\text{FeA}}\hat{S}_{\text{FeB}}, \quad (1)$$

where J is the magnetic exchange constant, a negative (positive) sign of it indicating an antiferromagnetic (ferromagnetic) exchange coupling. The local spin operators, *i.e.* \hat{S}_A and \hat{S}_B , are associated to the sites A and B, respectively, with the corresponding quantum numbers S_A and S_B .

Assuming the validity of Heisenberg's model for the specific spin-coupled system of interest, the generalized formula for calculating J using the broken-symmetry approach within the Kohn–Sham density functional theory can be derived as

$$J = \frac{[E^{\text{BS}} - E^{\text{HS}}]}{4S_A S_B + \sum_i \sum_j f_i^\alpha f_j^\beta |S_{ij}^{\alpha\beta}|^2}, \quad (2)$$

where E^{BS} and E^{HS} are the (total electronic) energies of the individual BS and HS Kohn–Sham determinants for the same configuration of all atoms in the system; $S_{ij}^{\alpha\beta}$ is the overlap between the Kohn–Sham spin orbitals $\psi_i^\alpha/\psi_j^\beta$ in the BS

determinant, f_i^α/f_j^β are their occupation numbers, and n is the number of electrons.^{23,24}

2.2 Multideterminant *ab initio* molecular dynamics

Though the broken-symmetry approach rejoices a great success in computing magnetic exchange couplings of molecular systems within static frameworks, it should be re-emphasized that the BS determinant by itself is a rather poor approximation of the true LS state. However, the (total electronic) energy of the LS state can be reasonably well approximated by a linear combination of the energies of the BS and HS determinants *via*

$$E^{\text{LS}} = (1 + c)E^{\text{BS}} - cE^{\text{HS}} \quad (3a)$$

where the coefficient c is given as

$$c = \frac{S_{\text{max}} - S_{\text{min}} - \sum_i \sum_j f_i^\alpha f_j^\beta |S_{ij}^{\alpha\beta}|^2}{4S_A S_B + \sum_i \sum_j f_i^\alpha f_j^\beta |S_{ij}^{\alpha\beta}|^2}. \quad (3b)$$

In other words, E^{LS} provides one with an approximate potential energy surface which can be used for structure optimization and molecular dynamics. Moreover, J computed according to eqn (2), which is obtained at no overhead cost once E^{LS} is known from eqn (3a) and (3b) for a given configuration, provides one with the consistent coupling constant given either an optimized structure or along a molecular dynamics trajectory. This method has been called the “extended broken-symmetry” (EBS) approach and amounts to an approximate spin-projection correction within a fully coupled two-determinant approach.^{23,24} Following our earlier work,^{23–26} we compute J and E^{LS} consistently in the so-called “strong localization” limit, thus assuming no overlap of the magnetic orbitals,²⁴ which leads to a coefficient c that is independent of both atom positions and electronic orbitals.

Given such a functional, *i.e.* eqn (3a) with eqn (3b), the forces acting on the nuclei can be calculated straightforwardly from

$$\nabla_{\mathbf{R}_i} E^{\text{LS}} = [1 + c]\nabla_{\mathbf{R}_i} E^{\text{BS}} - c\nabla_{\mathbf{R}_i} E^{\text{HS}} \quad (4)$$

for the approximate LS state. Using this equation one can readily perform structure optimizations, vibrational analysis, and AIMD (either using Car–Parrinello or Born–Oppenheimer propagation)²² on the approximate LS potential energy surface.^{23,24} Importantly, note that within this EBS approach, spin projection is not only applied when J is computed, as conventionally done in static calculations of such exchange constants, but it is already taken consistently into account upon structure optimizations as well as during molecular dynamics. In this way an overall consistent incorporation of spin projection in both the generation and analysis of the approximate antiferromagnetic ground state is realized.

2.3 Spin-constrained two-determinant *ab initio* molecular dynamics

Within spin-constrained density functional theory (CDFT), the cofactor is divided into two subregions A and B, localized at the

two spin centers A and B in the binuclear [2Fe-2S] complex, while the bridging atoms are excluded from these regions. The spin constraints can be defined in real space as

$$\int_A \rho^{\alpha\beta}(\mathbf{r})d\mathbf{r} = N_A, \quad \int_B \rho^{\alpha\beta}(\mathbf{r})d\mathbf{r} = N_B, \quad (5)$$

where $\rho^{\alpha\beta}(\mathbf{r})$ is the spin density

$$\rho^{\alpha\beta}(\mathbf{r}) = \rho^\alpha(\mathbf{r}) - \rho^\beta(\mathbf{r})$$

and N_A and N_B are the constraint values of the total number of unpaired electrons in subregions A and B, respectively; ideally, $|N_A| = 2S_A$ and $|N_B| = 2S_B$. For performing CDFT calculations within the two-determinant EBS scheme, thus leading to our spin-constrained two-determinant extended broken symmetry (CEBS) approach^{9,21} one needs to apply the spin density constraints independently to both the BS and HS determinants. In practice, one introduces two Lagrangian multipliers λ_A and λ_B and minimizes the functional

$$W[\rho^\alpha, \rho^\beta, \lambda_A, \lambda_B] = E^{\text{KS}}[\rho^\alpha, \rho^\beta] + \lambda_A \left(\int_A \rho^{\alpha\beta}(\mathbf{r})d\mathbf{r} - N_A \right) + \lambda_B \left(\int_B \rho^{\alpha\beta}(\mathbf{r})d\mathbf{r} - N_B \right) \quad (6)$$

subject to the imposed spin density constraints that act independently on the BS and HS determinants.

For practical convenience in selecting subregions A and B, and also for the estimation of accurate analytical nuclear forces, Löwdin charges on atoms in these regions are used to evaluate the total number of unpaired electrons, thus replacing the definition eqn (5) of subregions in real space.^{18,30–33} More recently, spatial partitioning schemes have also been implemented efficiently within CDFT by using Hirshfeld charges.^{34,35}

2.4 Validity of the CEBS approach and adiabatic AIMD

One might wonder how reliable the results of the present adiabatic AIMD simulations based on our CEBS approach for the LS ground state can be. This question arises in particular since in a most recent paper³⁶ the validity of the Heisenberg model for the low-lying spin states of Fe-S clusters was questioned. Assuming the validity of Heisenberg's model for the particular antiferromagnetic complex of interest is fundamental to the idea of carrying out spin-projection within rather simple two-determinant approaches such as EBS, as discussed in depth in ref. 24. Our own CAS-CI calculations, both for the ferredoxin and the Rieske cofactor, have shown that the Heisenberg model is perfectly valid as long as a common set of molecular orbitals is used for all spin states, obtained for instance by a state-averaged CAS-SCF calculation.

In the more accurate modified CAS-CI calculations,³⁷ however, deviations from the Heisenberg model are found. They are quantified in Table 1 where we compile the low-lying energy levels of the different spin states for the ferredoxin and Rieske-type cofactor models; for both systems the CEBS equilibrium structures were used in conjunction with state-averaged CAS-SCF orbitals and relaxation energies of 15.0 and 13.6 eV, respectively,

Table 1 Energies and antiferromagnetic exchange coupling constants obtained from the present modified CAS-CI calculations (see text) for the ferredoxin and Rieske-type model complexes. The total spin of the energy level, the associated energy (in cm^{-1} relative to the LS state), and the J values (in cm^{-1}) as determined from the difference between subsequent energies assuming validity of Heisenberg's model (see text) are reported as indicated. The J values in bold are obtained from $(E_{S=5} - E_{S=0})/30$

S	Ferredoxin		Rieske	
	E_S	$-J$	E_S	$-J$
0	0	175.7	0	182.1
1	351.4	178.8	364.1	185.2
2	1066.4	183.9	1105.1	190.5
3	2169.7	191.3	2248.1	197.8
4	3699.9	200.6	3830.3	206.0
5	5705.7		5890.0	
		190		196

as used earlier.⁹ We recall that in the present case the energy differences between the states with total spin $S = 0, 1, 2, 3, 4$ and 5 according to the perfect Heisenberg spin ladder are $2J, 4J, 6J, 8J$, and $10J$, respectively, which allows one to extract J values for instance from subsequent energy levels, as reported in Table 1. Clearly, there is an error in the order of 10% with respect to the prediction according to the ideal spin ladder, which still is fair agreement given the simplicity of the Heisenberg model. It is noted in passing that this is fully in line with the recently reported accurate results,³⁶ where also only slight deviations from the Heisenberg model were found for an oxidized [2Fe-2S] model complex.

Moreover, our particular (spin-constrained spin-projected two-determinant) CEBS approach²¹ that we use here has been benchmarked and validated earlier for both ferredoxin²¹ and Rieske⁹ complexes. Our underlying (spin-projected two-determinant) EBS approach^{23,24} itself, in particular after appropriately taking care of the self-interaction error,²⁵ has been demonstrated by us²⁵ and subsequently also by others²⁰ to provide a useful accuracy for iron-sulfur complexes and even for mixed-valence compounds.²⁰

Last but not least, it is worth stressing that it is perfectly justified to neglect excited spin states and thus to perform the CEBS AIMD simulations adiabatically in a single state, namely using the LS potential energy surface of the ground state according to eqn (3a). The reason is that the lowest excited state is about $2|J| \approx 400 \text{ cm}^{-1}$ above the ground state in the region of the equilibrium structure. This corresponds to a thermal energy ($k_B T \approx 600 \text{ K}$) which is about twice the temperature used in our simulations (300 K). This makes non-adiabatic coupling effects and thus multistate reactivity issues very unlikely to be of crucial importance.

We are therefore confident that all our conclusions concerning the various infrared absorption spectra and the differences in the magnetostructural dynamics between ferredoxin and Rieske-type cofactors are justified.

2.5 Technical details of the AIMD simulations

The AIMD simulations were performed on Rieske and ferredoxin model systems *in vacuo* as shown in the insets of Fig. 1

using our in-house modified CEBS version²¹ of the CPMD program package.³⁸ We have applied our CEBS approach using the Perdew–Burke–Ernzerhof (PBE) exchange–correlation functional for the calculation of the BS and HS determinants using a plane waves pseudopotential approach with a kinetic energy cutoff of 25 Ry and a periodic cubic box of length 20.1 Å. The atomic core electrons were represented using ultra-soft pseudopotentials where additional d-projectors for sulfur, scalar relativistic corrections, and semi-core states for iron were considered.

The constraints on the spin densities in the subregions A and B for ferredoxin were taken from our previous work on ferredoxin.²¹ However, applying the CEBS method to the Rieske cofactor is more involved since it has two chemically nonequivalent iron atoms for which the spin populations are slightly different from each other because of the different covalent bonding environment. We have also noticed that these populations are furthermore different for the BS and HS states. As a result, we have used four separate constraint values that were determined by adopting the quasi-self-consistent approach as described earlier.²¹

The iron–sulfur cofactors were initially equilibrated at 300 K for 3 ps, using a Nosé–Hoover chain thermostat, previous to 8 ps long NVT trajectories calculated to generate microcanonical dynamics which allows us to determine the magnetostructural auto- and cross-correlations. However, when we analyzed the J spectrum and compared it with our previous studies on ferredoxin, we realized that a single trajectory using CEBS inadequately sampled the phase space. As a result, the simulations could not

capture some of the crucial low-frequency resonances that characterize the J spectra at THz frequencies. Thus, in order to properly sample the relevant parts of phase space we performed five additional NVE simulations for each [2Fe–2S] cofactor. These NVE simulations were initialized from five (well separated but randomly chosen) phase space configurations generated by the NVT simulations at 300 K and thus yield observables in the canonical ensemble after averaging. This procedure was applied both for the Rieske and ferredoxin model complexes and all quantities presented have been obtained by averaging over all NVE runs for each model.

3 Results and discussion

3.1 Distribution of the magnetic coupling constant

The trajectory-averaged probability distribution functions $P(J)$ of the antiferromagnetic exchange coupling constant J are plotted in Fig. 1 for the ferredoxin and Rieske model complexes in panels (a) and (b), respectively. The maxima of the distributions are nearly identical in value for the two complexes, being -214 cm^{-1} for ferredoxin and -218 cm^{-1} for the Rieske model complex. This is in qualitative agreement with experimental results which show no significant differences between the J values for ferredoxins and Rieske proteins, though the experimental values in the protein matrix are slightly lower (being in the range of about -160 to -180 cm^{-1}) than those obtained by our CEBS AIMD simulations. Previously, we have determined the vacuum-to-protein shift²⁵ for the very same ferredoxin complex at 300 K *in vacuo* as that shown in the inset of Fig. 1 to the ferredoxin cofactor in Anabaena Fd protein at 300 K to amount to about -30 cm^{-1} , which brings the herein computed CEBS values into perfect agreement with experimental average J values. Similarly, also the widths of the probability distribution functions, and thus the thermal fluctuations at ambient conditions, are nearly identical for the ferredoxin and Rieske complexes.

At first glance it is quite surprising to find out that the J values for ferredoxins and Rieske cofactors are so similar, but one has to keep in mind that the experimental values are time averages and thereby do not contain detailed information on the microscopic dynamics and on the fluctuations of J . The latter, however, might very well be different for the chemically asymmetric and symmetric environments of the Rieske and ferredoxin complexes, respectively. Only a time (cross-) correlation analysis of the CEBS AIMD trajectories is able to extract the dynamical behavior of the magnetic properties and their explicit dependence on the structural dynamics by providing direct access to magnetostructural dynamics.^{23,24}

3.2 Dynamical magnetic properties

To study the dynamical behavior of a classical observable O , first of all a auto-correlation function is defined such as

$$G_{OO}(t) = \frac{\langle O(t_0)O(t_0+t) \rangle_{t_0}}{\langle O(t_0)O(t_0) \rangle_{t_0}}, \quad (7)$$

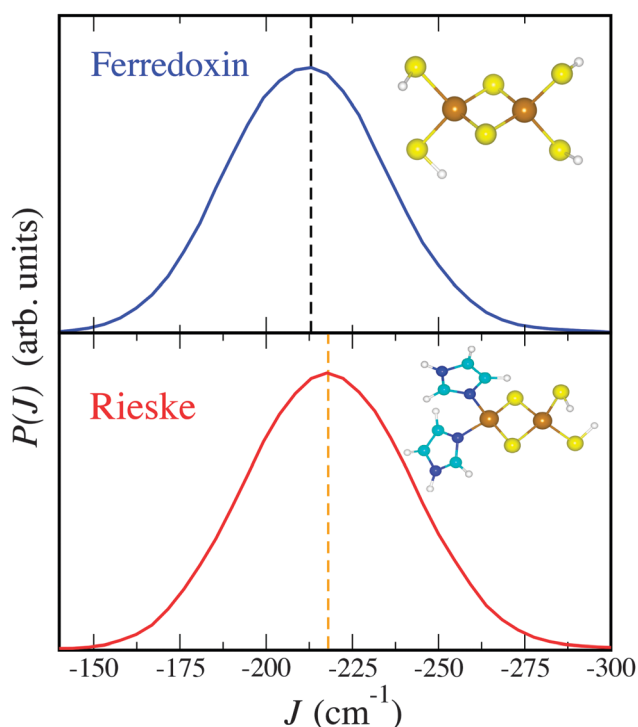


Fig. 1 Probability distribution functions $P(J)$ of the antiferromagnetic exchange coupling constants J at 300 K for the ferredoxin and Rieske [2Fe–2S] model complexes as shown in the insets.

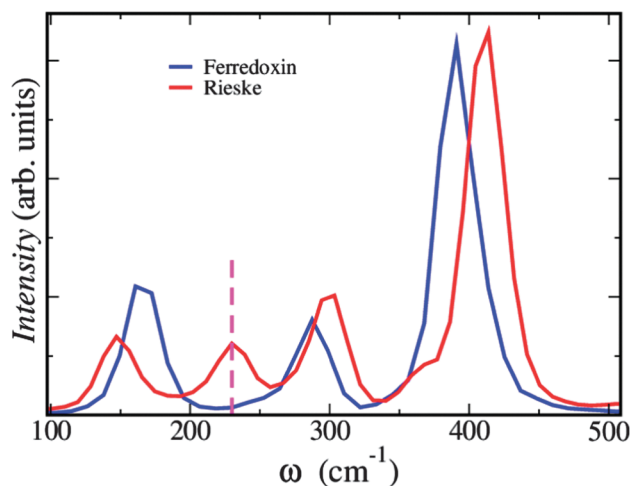


Fig. 2 Absorption spectra $A_{JJ}(\omega)$ from the dynamics of the antiferromagnetic exchange coupling constants $J(t)$ at 300 K for the ferredoxin (blue) and Rieske (red) [2Fe–2S] model complexes.

where $\langle \dots \rangle_{t_0}$ indicates the average over the reference time points t_0 along the trajectory generated in the MD simulations. The Fourier transform of this time correlation function,

$$G_{OO}(\omega) = \frac{1}{2\pi} \int_{-\infty}^{+\infty} G_{OO}(t) \exp[-i\omega t] dt, \quad (8)$$

represents the spectral density or ‘power spectrum’ associated to the corresponding property O . A quantity that can be shown to be directly related to the corresponding ‘absorption spectrum’ is defined as

$$A_{OO}(\omega) = \omega^2 G_{OO}(\omega), \quad (9)$$

which includes the so-called harmonic quantum correction factor for response functions (see ref. 23 and 24 for background) apart from various constants all set to unity. Similarly, cross-correlation spectra involving different observables O and O' are defined *via*

$$A_{OO'}(\omega) = \omega^2 G_{OO'}(\omega). \quad (10)$$

In order to dissect the magnetostructural dynamics of the two cofactor models we auto- and cross-correlate the time-dependent exchange coupling constant $J(t)$ and selected bond-length distances $d(t)$ to be specified at a later stage.

The time correlation function analyses of the exchange coupling constants $J(t)$ were performed for all *NVE* trajectories separately, both for the ferredoxin and Rieske complexes. Subsequently, the individual absorption spectra were averaged with equal weights to yield the final $A_{JJ}(\omega)$ spectra which are displayed in Fig. 2.

The $A_{JJ}(\omega)$ spectrum of ferredoxin consists in the region between 100 and 500 cm^{-1} , which is dominated by the vibrations of the iron–sulfur core, of three distinct peaks at about 160, 288 and 390 cm^{-1} . For the Rieske complex, in stark contrast, there are four such pronounced peaks at ≈ 149 , 230, 300 and 413 cm^{-1} in this region according to Fig. 2. The striking difference is that the observed peak at 230 cm^{-1} in

the Rieske cofactor model is completely absent in ferredoxin. The other three peaks are rather similar, both in their positions and intensities. The main difference is that the two high-frequency peaks of ferredoxin are shifted to slightly higher frequencies in the Rieske complex, from 288 to 300 cm^{-1} and from 390 to 413 cm^{-1} , respectively. A reversed trend is observed for the low-frequency peak that appears at 149 cm^{-1} in the Rieske complex while it is located at 160 cm^{-1} in ferredoxin.

This comparison of the absorption spectra $A_{JJ}(\omega)$ obtained from the auto-correlations of the time-dependent coupling constant $J(t)$ reveals that the dynamics of the magnetic properties is indeed very different between Rieske and ferredoxin cofactor models, albeit their time-averaged distribution functions $P(J)$ and thus their thermal averages $\langle J \rangle$ are nearly indistinguishable. Obviously the question now arises why the corresponding peak at 230 cm^{-1} is absent in ferredoxin?

3.3 Cross-correlation analyses: magnetostructural dynamics

In order to understand the origin of the various spectral features in the absorption spectra $A_{JJ}(\omega)$ as shown in Fig. 2 and, in particular, the difference between the Rieske complex and ferredoxin, we have performed a cross-correlation analysis of the dynamics involving the antiferromagnetic coupling constant, $J(t)$, and important structural parameters that describe of the iron–sulfur core. The latter have been selected bond lengths, interatomic distances, as well as bond angles. Since we are mainly interested to understand the stark differences in the $A_{JJ}(\omega)$ spectra of Rieske *versus* ferredoxin [2Fe–2S] complexes, we have only considered the dynamical fluctuations of the key structural parameters X defining the structure of the [2Fe–2S] core and moreover the covalent bonds to the next neighbors of the two Fe atoms which connect the cofactors to the protein residues. These parameters are the bond angle α , the four bridging Fe–S bond distances in the core, $d_{\text{Fe-S}_b}$, and the two terminal bond distances $d_{\text{Fe-S}_t}/d_{\text{Fe-N}_t}$ between the Fe sites and the terminal S/N atoms of the cysteine and histidine ligands, respectively.

The set of absorption and cross-correlation spectra, *i.e.* $A_{dd}(\omega)$ and $A_{Jd}(\omega)$, for the different bond lengths d in the two cofactor models as well as $A_{JJ}(\omega)$ for reference are depicted in Fig. 3. The spectra involving the bond angle α are not included since the respective $A_{\alpha\alpha}(\omega)$ turn out to be nearly identical for the Rieske and ferredoxin complexes and are thus irrelevant for rationalizing the differences in the magnetostructural dynamics of the two cofactors. The absorption spectra have peaks at about 150 cm^{-1} and the corresponding cross-correlations $A_{Jd}(\omega)$ are very small in the whole frequency region.

3.3.1 Ferredoxin cofactor model. The $A_{dd}(\omega)$ spectra for the bond distances d in Fig. 3(a) show that the vibrational modes in the region around 400 cm^{-1} consist mainly of the four internal bond distances $d_{\text{Fe-S}_b}$ between the Fe centers and the bridging S atoms. Thus, only small contributions are due to the dynamics of the terminal Fe–S_t distances in this frequency range. In the region between 250 and 350 cm^{-1} , on the other hand, it is the vibrations of the terminal Fe–S_t bonds that dominate, but with non-negligible contributions from dynamical couplings to the

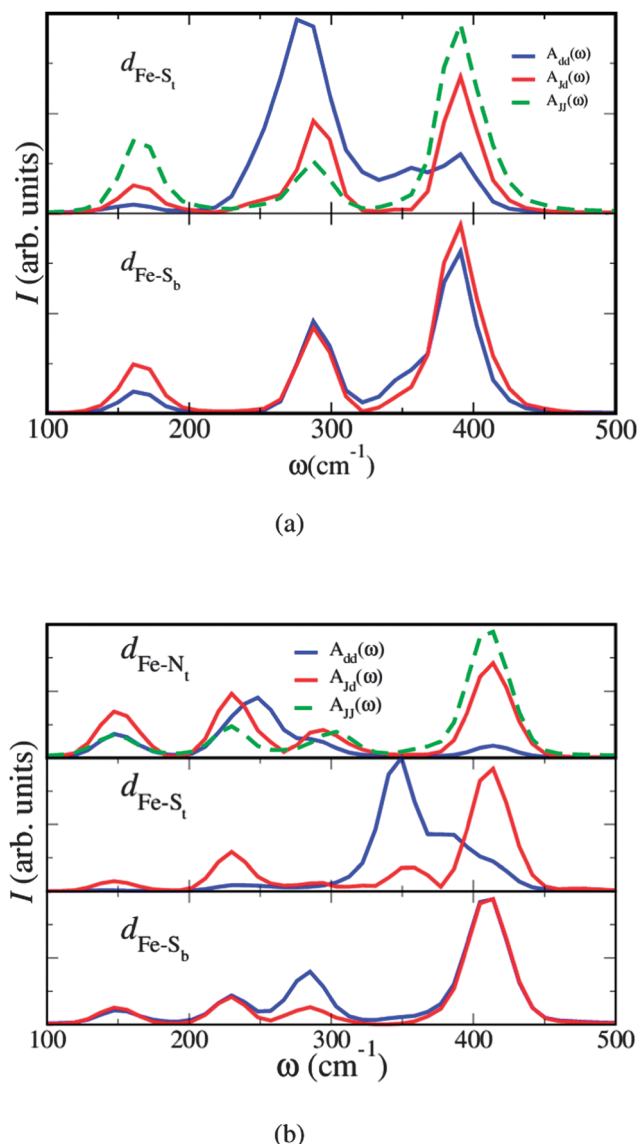


Fig. 3 Absorption spectra $A_{JJ}(\omega)$, bond length vibrational spectra $A_{dd}(\omega)$, and corresponding cross-correlation spectra $A_{Jd}(\omega)$ from the dynamics of the antiferromagnetic exchange coupling constants $J(t)$ and $d(t)$ at 300 K for the (a) ferredoxin and (b) Rieske [2Fe-2S] model complexes where $d(t)$ is given by $d_{\text{Fe-S}_t}$, $d_{\text{Fe-S}_b}$, and $d_{\text{Fe-N}_t}$ (see text).

internal Fe-S_b distances. This is completely in line with the computational analysis⁹ of the resonance Raman spectra for several ferredoxin containing proteins^{39–41} as well as with our own previous spectral decomposition^{23,24} for the same Fe₂S₄H₂ model complex. The cross-correlation spectra $A_{Jd}(\omega)$ indicate that there is a nearly perfect correlation between J and the modes involving the iron bonds to the bridging sulfurs, $d_{\text{Fe-S}_b}$, while the corresponding correlation between the exchange constant and the terminal iron-sulfur bonds, $d_{\text{Fe-S}_t}$, is much weaker.

The absorption spectrum of J , $A_{JJ}(\omega)$, in the upper panel of Fig. 3(a), is dominated by the vibrational modes containing $d_{\text{Fe-S}_b}$, in particular the A_g mode at about 400 cm⁻¹ (see ref. 23 and 24 for the assignment), while both bridging and terminal

Fe-S bond distances contribute to the peak at 288 cm⁻¹. The peak at 160 cm⁻¹ is mainly caused by the A_g mode of the bond angle α in the iron-sulfur core, *i.e.* the “angular” mode.^{23,24}

All this analysis means that the fluctuations of the anti-ferromagnetic exchange coupling constant $J(t)$ are mainly a consequence of the vibrational dynamics of the bond distances in the [2Fe-2S] core itself and to a much smaller extent of the fluctuations involving the terminal ligands.

3.3.2 Rieske cofactor model. The situation is more complex for the Rieske complex as analyzed in Fig. 3(b). The position of the high-frequency peak in the spectrum of J , $A_{JJ}(\omega)$, is similar to that of the corresponding resonance in ferredoxin at 390 cm⁻¹, being only shifted by about 20 cm⁻¹ to 413 cm⁻¹. This is to be expected since this vibrational resonance is due to the A_g mode of the bond distances in the iron-sulfur core and the average Fe-S_b bond distances in ferredoxin and the Rieske model complex being nearly identical, 2.25 and 2.26 Å, respectively. Note that our CEBS AIMD simulations yield for $d_{\text{Fe-N}_t}$ and $d_{\text{Fe-S}_b}$ average values of 2.20 and 2.32 Å, respectively, which are the values reported earlier in ref. 9. Similarly, the peak at 149 cm⁻¹ corresponding to the “angular” mode is also very close to the corresponding resonance in ferredoxin.

In the intermediate frequency range, however, *i.e.* between 200 and 350 cm⁻¹, there are pronounced differences observed between ferredoxin and the Rieske complex which can be viewed to be the “fingerprint region” that allows one distinguish these two distinct cofactors. The absorption spectra $A_{dd}(\omega)$ for the structural parameters d as well as the cross-correlation spectra $A_{Jd}(\omega)$ show how the ferredoxin peak at 288 cm⁻¹ is split into two parts in the Rieske case. The part at 230 cm⁻¹ is essentially caused by the fluctuations of the terminal bond distances $d_{\text{Fe-N}_t}$ between Fe and N atoms, thus involving mainly the two histidine residues absent in ferredoxins, with only small contributions from both the terminal and bridging Fe-S distances $d_{\text{Fe-S}_t}$ and $d_{\text{Fe-S}_b}$. The terminal Fe-S_t vibrational modes, on the other hand, are shifted to higher frequencies and are responsible for the small shoulder at about 360 cm⁻¹ that is visible in the $A_{JJ}(\omega)$ spectrum shown in Fig. 2. Finally, due to the chemical asymmetry of the Rieske iron-sulfur core resulting into different Fe-S_b bond lengths, the contribution of the internal [2Fe-2S] core vibrations is split into two smaller parts, one of which is still located at 300 cm⁻¹ as in ferredoxin while the other one occurs at about 225 cm⁻¹ and enforces the peak at about 230 cm⁻¹.

4 Conclusions and outlook

The two iron atoms in the [2Fe-2S] cofactors of ferredoxins and Rieske-type proteins are antiferromagnetically coupled. The magnitude of the measured exchange coupling constants, J , are rather similar in the two types of proteins, about 180 cm⁻¹. This is slightly surprising since the chemical asymmetry of the [2Fe-2S] core in the Rieske-type proteins should have the consequence that their properties are different from those of the ferredoxins possessing symmetric [2Fe-2S] cores. Such

differences have been indeed found for the structures of the iron–sulfur cores⁹ and the resonance Raman spectra.^{39–41}

The present *ab initio* molecular dynamics simulations, which rely on a spin-projected density functional representation of the underlying electronic structure in terms of two coupled spin-constrained Kohn–Sham determinants, could resolve this dilemma. This dynamical method directly provides access to the time-evolution of the coupling constant, $J(t)$, and thereby allows one to extract detailed information about the magnetostructural dynamics of ferredoxin and Rieske model complexes *in vacuo* at 300 K. The absorption spectrum obtained from the auto-correlations of $J(t)$, $A_{JJ}(\omega)$, shows for the ferredoxin complex three prominent peaks in the region between 100 and 500 cm^{−1}, which is the range that is known to be dominated by the internal and terminal vibrational modes of the [2Fe–2S] core. In the Rieske-type complex, on the other hand, $A_{JJ}(\omega)$ exhibits four peaks in this region. The low and high frequency peaks, at about 150 and 400 cm^{−1}, are rather similar in the two [2Fe–2S] containing complexes. But the ferredoxin peak in the intermediate frequency regime, between about 200 and 350 cm^{−1}, is shown to be split in the Rieske complex into two parts. This is thus a “fingerprint region” that allows one to distinguish these two distinct cofactors.

Power spectra of several structural parameters $X(t)$ involved, mainly the Fe–S distances, as well as detailed cross-correlation analyses of their fluctuations with respect to the dynamics of the exchange coupling constant itself, $A_{JX}(\omega)$, reveal that this splitting is indeed directly caused by the chemical asymmetry of the [2Fe–2S] core in the Rieske complex. This is completely in line with the experimental resonance Raman spectra showing several more peaks in this region for Rieske than for ferredoxin proteins.^{39–41} In stark contrast, the calculated time average of the coupling constant, $\langle J \rangle$, turns out to be essentially the same for the ferredoxin and Rieske complex, in substantial agreement with the experimental data for the corresponding proteins.

The present study shows most clearly that it needs a detailed dynamical analysis to reveal the differences in the magnetic properties of ferredoxins and Rieske-type proteins. Conventional magnetic measurements, yielding only time averages, are not sufficient to capture the details of the magnetostructural dynamics in these iron–sulfur proteins. Unfortunately, such measurements of $A_{JJ}(\omega)$ or $A_{JX}(\omega)$ are not yet available. We hope that advanced spectroscopic methods, possibly combining Mößbauer and vibrational measurements of the [2Fe–2S] cofactors as already outlined in ref. 23, might be developed in the future. In particular, frequency-dependent excitations with a focus on the dynamics of Fe sites could be achieved by nuclear inelastic scattering of synchrotron radiation at Mößbauer-active nuclei, which is already established for intramolecular vibrational spectroscopy that is sensitive exclusively to modes that involve the motion of iron nuclei.^{42,43} Although challenging, such an experimental technique would open up a new dimension by revealing the rich magnetostructural dynamics not only of such iron-containing cofactors in metalloproteins, but also of magnetic complexes in general.

Acknowledgements

Md. E. Ali is thankful to a support by the Alexander von Humboldt-Foundation *via* his Humboldt Postdoctoral Fellowship and D.M. acknowledges partial financial support from DFG. The calculations were carried out using resources from NIC (Jülich), RV-NRW, and BOVILAB@RUB.

References

- 1 J. A. Fee, K. L. Findling, T. Yoshida, R. Hille, G. E. Tarr, D. O. Hearshen, W. R. Dunham, E. P. Day, T. A. Kent and E. Munck, *J. Biol. Chem.*, 1984, **259**, 124–133.
- 2 S. Iwata, M. Saynovits, T. Link and H. Michel, *Structure*, 1996, **4**, 567–579.
- 3 E. J. Leggate, E. Bill, T. Essigke, G. M. Ullmann and J. Hirst, *Proc. Natl. Acad. Sci. U. S. A.*, 2004, **101**, 10913–10918.
- 4 D. C. Johnson, D. R. Dean, A. D. Smith and M. K. Johnson, *Annu. Rev. Biochem.*, 2005, **74**, 247–281.
- 5 D. J. Kolling, J. S. Brunzelle, S. Lhee, A. R. Crofts and S. K. Nair, *Structure*, 2007, **15**, 29–38.
- 6 R. Lill, *Nature*, 2009, **460**, 831–838.
- 7 H. T. Tsang, C. J. Batie, D. P. Ballou and J. E. Penner-Hahn, *Biochemistry*, 1989, **28**, 7233–7240.
- 8 R. Morales, M.-H. Charon, G. Hudry-Clergeon, Y. Pétillot, S. Norager, M. Medina and M. Frey, *Biochemistry*, 1999, **38**, 15764–15773.
- 9 Md. E. Ali, N. N. Nair, M. Retegan, F. Neese, V. Staemmler and D. Marx, *J. Biol. Inorg. Chem.*, 2014, **19**, 1287–1293.
- 10 L. Noodleman, D. Case and A. Aizman, *J. Am. Chem. Soc.*, 1988, **110**, 1001–1005.
- 11 A. Bassan, M. R. A. Blomberg, T. Borowski and P. E. M. Siegbahn, *J. Phys. Chem. B*, 2004, **108**, 13031–13041.
- 12 M. Shoji, K. Koizumi, Y. Kitagawa, S. Yamanaka, M. Okumura and K. Yamaguchi, *Int. J. Quantum Chem.*, 2007, **107**, 609–627.
- 13 J. Ballmann, A. Albers, S. Demeshko, S. Dechert, E. Bill, E. Bothe, U. Ryde and F. Meyer, *Angew. Chem., Int. Ed.*, 2008, **47**, 9537–9541.
- 14 A. M. Kuznetsov, E. M. Zueva, A. N. Masliy and L. I. Krishtalik, *Biochim. Biophys. Acta, Bioenerg.*, 2010, **1797**, 347–359.
- 15 A. Albers, S. Demeshko, S. Dechert, C. T. Saouma, J. M. Mayer and F. Meyer, *J. Am. Chem. Soc.*, 2014, **136**, 3946–3954.
- 16 W. Geertsma and D. Khomskii, *Phys. Rev. B*, 1996, **54**, 3011–3014.
- 17 J. A. McCleverty and M. D. Ward, *Acc. Chem. Res.*, 1998, **31**, 842–851.
- 18 I. Rudra, Q. Wu and T. V. Voorhis, *J. Chem. Phys.*, 2006, **124**, 024103.
- 19 J. R. Schmidt, N. Shenvi and J. C. Tully, *J. Chem. Phys.*, 2008, **129**, 114110.
- 20 D. Bovi and L. Guidoni, *J. Chem. Phys.*, 2012, **137**, 114107.
- 21 Md. E. Ali, N. N. Nair, V. Staemmler and D. Marx, *J. Chem. Phys.*, 2012, **136**, 224101.

- 22 D. Marx and J. Hutter, *Ab Initio Molecular Dynamics: Basic Theory and Advanced Methods*, Cambridge University Press, Cambridge, 2009.
- 23 E. Schreiner, N. N. Nair, R. Pollet, V. Staemmler and D. Marx, *Proc. Natl. Acad. Sci. U. S. A.*, 2007, **104**, 20725–20730.
- 24 N. N. Nair, E. Schreiner, R. Pollet, V. Staemmler and D. Marx, *J. Chem. Theory Comput.*, 2008, **4**, 1174–1188.
- 25 N. N. Nair, J. Ribas-Arino, V. Staemmler and D. Marx, *J. Chem. Theory Comput.*, 2010, **6**, 569–575.
- 26 S. A. Fiethen, V. Staemmler, N. N. Nair, J. Ribas-Arino, E. Schreiner and D. Marx, *J. Phys. Chem. B*, 2010, **114**, 11612–11619.
- 27 L. Noodleman, *J. Chem. Phys.*, 1981, **74**, 5737–5743.
- 28 L. Noodleman and E. R. Davidson, *Chem. Phys.*, 1986, **109**, 131–143.
- 29 L. Noodleman, C. Peng, D. Case and J.-M. Mouesca, *Coord. Chem. Rev.*, 1995, **144**, 199–244.
- 30 Q. Wu and T. Van Voorhis, *Phys. Rev. A*, 2005, **72**, 024502.
- 31 I. Rudra, Q. Wu and T. Van Voorhis, *Inorg. Chem.*, 2007, **46**, 10539–10548.
- 32 T. Van Voorhis, T. Kowalczyk, B. Kaduk, L.-P. Wang, C.-L. Cheng and Q. Wu, *Annu. Rev. Phys. Chem.*, 2009, **61**, 149–170.
- 33 B. Kaduk, T. Kowalczyk and T. Van Voorhis, *Chem. Rev.*, 2012, **112**, 321–370.
- 34 H. Oberhofer and J. Blumberger, *J. Chem. Phys.*, 2009, **131**, 064101.
- 35 H. Oberhofer and J. Blumberger, *J. Chem. Phys.*, 2010, **133**, 244105.
- 36 S. Sharma, K. Sivalingam, F. Neese and G. K.-L. Chan, *Nat. Chem.*, 2014, **6**, 927–933.
- 37 K. Fink and V. Staemmler, *Mol. Phys.*, 2013, **111**, 2594–2605.
- 38 J. Hutter *et al.*, CPMD, see www.cpmid.org.
- 39 D. Kuila, J. R. Schoonover, R. B. Dyer, C. J. Batie, D. P. Ballou, J. A. Fee and W. H. Woodruff, *Biochim. Biophys. Acta*, 1992, **1140**, 175–183.
- 40 F. A. J. Rotsaert, J. D. Pikus, B. G. Fox, J. L. Markley and J. Sanders-Loehr, *JBIC, J. Biol. Inorg. Chem.*, 2003, **8**, 318–326.
- 41 T. Iwasaki, T. Imai, A. Urushiyama and T. Oshima, *J. Biol. Chem.*, 1996, **271**, 27659–27663.
- 42 H. Paulsen, H. Winkler, A. X. Trautwein, H. Grönsteudel, V. Rusanov and H. Toftlund, *Phys. Rev. B*, 1999, **59**, 975–984.
- 43 H. Paulsen, V. Rusanov, R. Benda, C. Herta, V. Schünemann, C. Janiak, T. Dorn, A. I. Chumakov, H. Winkler and A. X. Trautwein, *J. Am. Chem. Soc.*, 2002, **124**, 3007–3011.